Towards electroformed nanostructured aluminum alloys with high strength and ductility

Shiyun Ruan[a)] and Christopher A. Schuh[b)]
Department of Materials Science & Engineering, Massachusetts Institute of Technology, Cambridge, Massachusetts 02139

Nanostructured Al–Mn alloys are proposed as high-strength low-density materials, which can be electroformed (i.e., produced electrolytically and removed from the substrate) from ionic liquid. A variety of current waveforms, including direct current (DC) and pulsed current (PC), are used to electrodeposit nanostructured Al–Mn alloys, with some PC methods producing significant improvements in film ductility. Transmission electron microscopy observations point to a number of structural advantages induced by PC that apparently ductilize the Al–Mn alloys: (i) grain refinement to the nanocrystalline range without the introduction of a competing amorphous phase, (ii) unimodal nanocrystalline grain size distribution, and (iii) more homogeneous structure. The significant increase in apparent ductility in the PC alloys is also apparently related to stress- or deformation-induced grain growth, which leads to alloys with unique combinations of specific hardness and film ductility.

I. INTRODUCTION

While most commercial Al alloys have the two very desirable properties of low density and high toughness, they exhibit sufficiently lower strength and hardness in comparison to heavier alloys (e.g., steels, nickel, and titanium alloys) that the weight savings they promise is often undermined by the need for greater load-bearing cross-sections. Recent research on nanocrystalline and amorphous Al alloys represents a promising new direction that could achieve substantially higher strength while maintaining the low density intrinsic to Al.[1–10] What is more, some results on nanocrystalline Al and its alloys reveal the possibility of plastic deformation up to ~10% in tension,[2,3] which bodes well for nanostructured alloys with acceptable fracture toughnesses. Plasticity in nano-structured alloys seems to be facilitated by low artifact and vacancy contents,[2] as well as grain sizes that are in the range of about ~10–100 nm, where dislocation- and grain boundary-mediated deformation mechanisms can operate simultaneously.[11–14] These results point to the importance of a synthesis route that can produce artifact-free and fully dense nanocrystalline alloys with tailorable grain sizes.

Techniques that have been developed to synthesize nanostructured alloys include high-energy milling,[15–18] other forms of severe deformation,[3,15,19,20] gas-phase synthesis,[15,21] chemical and physical vapor deposition,[15,19] magnetron sputtering,[15,22] and electrochemical deposition.[15,23–30] All these techniques are well developed from a research perspective, and some have achieved commercial application for niche product forms, especially, e.g., nanocrystalline coatings.[31] However, the production of freestanding bulk nanostructured materials presents particular challenges to the scalability of many of these techniques. Among them, electrolytic processing seems to possess the intrinsic qualities needed to achieve production of bulk nanostructured materials at full scale.

First, electrochemical deposition is particularly attractive for its large palette of easily adjustable processing variables, such as electrolyte composition, temperature, and applied current or voltage waveform; judicious adjustments to these parameters permit a fine level of control over the electrodeposited nanocrystalline grain size and deposit quality.[23,25,32] Second, whereas the term "electrodeposition" is widely used to connote a coating process or a laboratory method for thin film production, the electrolytic preparation of freestanding foils, sheets, and net shape objects up to several centimeters in thickness is also a common industrial process called "electroforming."[33,34]

Combining the demonstrated commercial successes of electrodeposited nanocrystalline thin coatings with the existence proof of scalability provided by the electroforming industry, we anticipate that the electrolytic route may in fact be a preferred one to achieve high-strength, high-toughness, low-density nanostructured alloys based on aluminum. In the case of aluminum and other reactive metals, however, there are additional challenges associated with electrodeposition from the nonaqueous solutions

---

[a)]Present address: Xtalic Corporation, 260 Cedar Hill Street, Marlborough, MA 01752, USA

[b)]Address all correspondence to this author.
  e-mail: schuh@mit.edu

required for those systems. Aluminum can be deposited from various electrolytes, including molten salts (generally at elevated temperatures),[35–37] and is currently industrially applied from electrolytes containing toluene.[38–41] In such solutions, a preliminary demonstration of the inherent scalability to an Al electroforming operation also exists.[42,43]

More recently, ionic liquids have been the subject of significant basic research focus for electrodeposition of Al.[44–46] In fact, in ionic liquid electrolytes, there has also been progress in the development of nanostructured aluminum deposits. For example, some authors have reported the use of grain refining additives, such as nicotinic acid and benzoic acid in chloroaluminate ionic liquid electrolytes[46,47] to produce essentially pure nanocrystalline aluminum. In our recent study,[48] we electrodeposited Al–Mn alloys from an ionic liquid electrolyte at room temperature and obtained a broad range of structures including microcrystalline, nanocrystalline, amorphous, and nanoquasicrystalline, with Mn generally promoting finer-scale structures and noncrystalline features. Those alloys were found to have very high hardness levels, even in excess of 3 GPa (i.e., a uniaxial strength level of order 1 GPa).

Despite the above progress in electrolytic synthesis of nanostructured Al and Al alloys, the existing studies to date have not yet established that these materials can simultaneously have high hardness and intrinsic toughness, nor identified specific electrolytic processing routes to optimize the nanostructure to achieve those properties. In the present work, we present a first study to address this issue, by first evaluating hardness and film ductility for conventional direct current (DC) electrodeposited Al–Mn alloys, for which detailed nanostructure characterization is already available in Ref. 48, and then exploring pulsed current (PC) deposition as a means of manipulating the mechanical properties of the deposit. Through this study, we demonstrate deposits with unique combinations of high strength and apparent ductility, a necessary step toward the ultimate goal of electroformed nanostructured Al alloys.

II. EXPERIMENTAL

A. Electrodeposition

The chloroaluminate ionic liquid used to electrodeposit the Al–Mn alloys in this study was synthesized from two precursors: 1-ethyl-3-methylimidazolium chloride and anhydrous aluminum chloride; this electrolyte was prepared using the same procedures detailed in Ref. 48. Anhydrous manganese chloride (>98% pure, from Aldrich, St. Louis, MO) was added to various levels to effect different solute compositions in the electrodeposited sheets. Electrodeposition experiments were carried out under galvanostatic conditions and a variety of current waveforms were used. These will be described in more detail in the sections that follow, but briefly, we explored two different types of applied current: DC and PC.

For all depositions, the anode material was 99.99% high purity aluminum sheet and the substrate material was rolled pure copper sheet (99.9%), electropolished to a mirror finish. Electrodeposition experiments were carried out at room temperature until film thicknesses of ∼10–15 μm were obtained; typical plating durations were of order 2–8 h, depending upon the current waveforms used.

B. Characterization

Scanning electron microscope (SEM; LEO Elektronenmikroskopie GmbH, Oberkochen, Germany) images of the deposits were obtained using a Leo 438VP SEM, and the chemical composition of each sample was quantified via calibrated energy dispersive x-ray analysis (EDX; X-ray Optics/AAT #31102). For all specimens analyzed in this study, only the Al and Mn peaks were observed in the EDX spectrum. It is however possible that other impurity elements were present at low quantities below the EDX detection threshold.

To prepare transmission electron microscopy (TEM) specimens, freestanding Al–Mn films were obtained by dissolving the copper substrates in concentrated nitric acid. The freestanding Al–Mn films were then twin-jet electropolished at 10 V in a 20% solution of perchloric acid in methanol at −60 °C. Selected alloy films were also ion milled at −80 °C with an ion accelerating voltage of 4 kV and source current of 4 mA (Fischione Model 1010, Fischione Instruments Inc, Export, PA). The TEM specimens were examined using two instruments: a JEOL 200CX and a JEOL 2010F, both of which were operated at 200 kV. The probe used to obtain the selected area diffraction patterns was 1 μm in diameter. Statistical analysis of the average grain size was carried out using both the bright-field and dark-field images; for each bright-field image, at least four corresponding dark-field images were obtained using the (111) and (200) reflections. These dark-field images were used to help identify the grains on the bright-field image, the sizes of which were measured by hand. The reported TEM grain sizes correspond to the diameter of a circle with an equivalent area. For each specimen, at least 200 grains were analyzed.

C. Mechanical testing

Some deposits were selected for mechanical testing. Micro-Vickers indentation tests were carried out using a 5-g load and a 15-s holding time, on Al–Mn film surfaces prepared by mechanical polishing at 600 and 800 grit, followed by decreasing grades of diamond paste (3 and 1 μm). The indentation depth was in all cases significantly less than one-tenth the film thickness, ensuring a clean bulk measurement. Each reported data point represents an average of at least eight indentations.

The guided bend test, as detailed in ASTM E290-97a (2004), was used to assess the film ductility of selected deposits. For this test, the film was left on the copper substrate, and the film and substrate were together bent over

a mandrel by pressing it into a mating jig. The thickness, t, of tested samples (i.e., film and copper substrate together) was measured using a micrometer and ranged from 0.2 to 0.5 mm, while the radii of the end of the mandrel, r, ranged from 0.127 to 1.397 mm. After the guided bend test, the convex bent surfaces were examined for cracks and fissures using the SEM.

For each bent sample, the thickness of the Al–Mn film was less than 10% that of the substrate. Thus, to a good approximation, the film laid on the outer fiber of the bent specimen and experienced a state of uniaxial tension. Assuming the neutral plane to lie in the center of the substrate plus film, the true tensile strain on the convex surface is given approximately as

$$\varepsilon = \ln\left(\frac{r/_t + 1}{r/_t + 1/_2}\right) \quad . \tag{1}$$

For each alloy tested in this way, multiple samples were produced and subjected to different amounts of tensile strain (through the use of different mandrels) during the guided bend tests. Strains between about 5 and 50% were achieved with this procedure. We define the "film ductility" by examining each alloy at a variety of strains and identifying the largest applied strain at which no cracks or fissures were observed on the bent film; the error bars on the film ductility values are given by the resolution provided by the various mandrels used in testing. In principle, the guided bend test as applied with the present geometry is equivalent to a uniaxial tensile test but with the film still supported on the substrate. It is likely that because the film is supported on a substrate, some flaws that are present on the film may be constrained from propagating, so the film ductility values we report are upper bound values as compared to what would be expected from an unconstrained tension test.

For some of the samples that remained uncracked after the bend test, their copper substrates were dissolved in concentrated nitric acid. Both the bent portions of the Al–Mn films, as well as the regions that were far from the bend, were jet polished for postmortem TEM analysis. Because samples that failed during the bend tests exhibited narrow cracks, the fracture surfaces were not sufficiently exposed for microscopic analysis. Thus, an Instron tensile tester (Instron, Norwood, MA) was used to fracture fresh specimens (film and substrate together) in tension. The fracture surfaces were analyzed in the JEOL 6700 SEM (Tokyo, Japan) at 5 kV.

III. DC ELECTRODEPOSITED Al–Mn ALLOYS

In our previous work, Al–Mn alloys with a wide variety of structures were electrodeposited at room temperature using conventional DC deposition, their structures were characterized, and their hardnesses measured.[48] In this section, we briefly revisit these deposits for several reasons.

First, the work in Ref. 48 did not address the film ductility of the DC deposits, so here, we have prepared new specimens following the same procedures to provide this data. Second, in a subsequent section, we will explore a variety of PC waveforms and their effect on the deposit properties; the DC specimens provide an important point of comparison. The DC deposits described below were all produced with waveform "A," as shown in Table I, i.e., an applied DC current density of 6 mA/cm^2, which is identical to that used in our prior work.[48] Herein, these alloys will be referred to as the "A" alloys.

A. Microstructure and hardness

For the DC "A" alloys, three structural regimes, defined by the alloy Mn content, were identified in Ref. 48, and the deposits produced in this work reproduce the same result. The alloy composition, phase composition, grain size, and hardness of these alloys, which were originally presented in Ref. 48, are summarized in Table II. Figure 1 shows TEM micrographs of the "A" alloys, also originally presented in Ref. 48; these micrographs will be used to provide a point of comparison with the microstructures obtained using the PC waveforms, which will be discussed in a later section.

TABLE I. Pulse parameters of waveforms used in this study.

Waveform	Pulse current density (mA/cm^2)		Pulse duration (ms)	
	i_1	i_2	t_1	t_2
"A" (DC)	6	6	20	20
"B"	6	3	20	20
"C"	6	1	20	20
"D"	6	0	20	20
"E"	6	−3	20	20
"F"	6	−3.75	20	20
"G"	6	−3	20	5
"H"	6	−3	20	10

TABLE II. Alloy composition, phase content, grain size, and hardness of the "A" alloys.[48]

Alloy composition (at.% Mn)	Phase content	Grain size	Hardness (GPa)
0	FCC	14 ± 4 μm	1.0
6.0		8 ± 3 μm	2.9
7.5		4 ± 2 μm	2.8
8.2[a]	FCC + amorphous	40 ± 10 nm	5.2
9.2		7 ± 3 nm	4.4
10.8		6 ± 2 nm	4.1
12.3		4 ± 1 nm	4.3
13.6	Amorphous	...	4.8
15.8		...	5.5

[a] This specimen exhibited a bimodal grain size distribution, including small grains of 3 ± 1 nm diameter; see Ref. 48.

These images illustrate the structural changes in DC deposits as their Mn content rises through three general regimes:

(i) 0 to ~8 at.% Mn: The alloys comprise microcrystalline FCC solid solutions. As the Mn content increases, the grain size decreases from 15 to 7 μm [Fig. 1(a)] and the hardness increases from about 1.0 to 2.8 GPa. The decrease in grain size with Mn content is apparently related to the kinetics of grain nucleation during the deposition process.

(ii) ~8 to 13 at.% Mn: These deposits comprise dual-phase structures, with nanometer-scale crystals of the FCC solid solution phase coexisting with an amorphous phase [Fig. 1(b)-1(e)]. The amorphous phase is Mn enriched,[48] and its volume fraction increases with the global Mn content. The phases are arranged as domains of one phase embedded in a network or matrix of the other; the characteristic radius of the domains is about 10–25 nm. These alloys exhibit high hardnesses above 3 GPa and a local peak in hardness of 5.2 GPa is observed in the 8.2 at.% Mn alloy, where the FCC phase is the majority phase.

(iii) Above ~13 at.% Mn: These alloys exhibit a single amorphous phase [Fig. 1(f)], whose hardness increases from 4.8 to 5.5 GPa as Mn content rises. The apparently amorphous phase contains preexisting nanoquasicrystalline nuclei in the as-deposited state; these nuceli grow into nanoquasicrystals at about 300 °C.[48]

In Ref. 48, we considered the effects of composition through this sequence of structural changes, and we observed that the microstructural features of DC electrodeposited Al–Mn alloys appeared to be governed by nucleation kinetics at the electrode. The phase distributions of the duplex alloys comprising nanocrystalline grains and the amorphous phase were plausibly related to adatom surface diffusion during electrodeposition, i.e., the characteristic length of phase separation was found to relate to the characteristic diffusion length of an adatom on the film surface.

B. Film ductility

The film ductility was measured for nanostructured and amorphous DC "A" alloys with two selected compositions, 8.2 and 13.6 at.% Mn. Figure 2 illustrates SEM images of the convex bent surfaces of these alloys upon application of ~5% tensile strain. Figure 2(a) and 2(c) shows that both alloys exhibit multiple cracks that propagate across the entire sample width. The corresponding higher magnification images on the right illustrate a high density of relatively straight cracks and no evidence of plastic flow in the uncracked ligaments. These are signatures of catastrophic brittle failure; the film ductility of these alloys falls below ~5% and may be assumed to be essentially zero.

That the amorphous 13.6 at.% Mn alloy exhibits low ductility is in line with catastrophic failure commonly observed in brittle amorphous alloys and bulk metallic glasses loaded in tension. Thus, it is also likely that the brittle amorphous phase in the nanostructured 8.2 at.% Mn contributes to its low toughness. As illustrated in Fig. 1(b), this two-phase alloy exhibits a bimodal grain size distribution centered at ~40 and ~3 nm. Since nanograins that are less than ~10 nm are considered incapable of dislocation
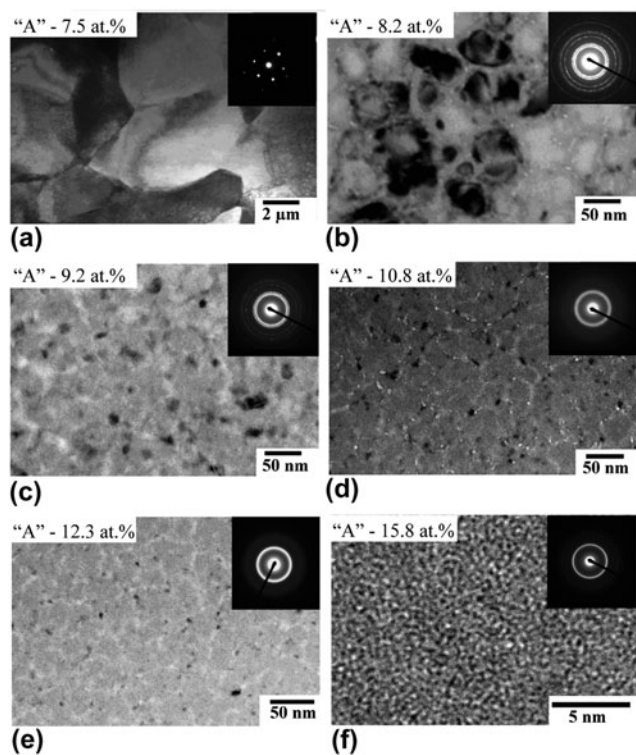

FIG. 1. Bright-field TEM images and electron diffraction patterns of alloys electrodeposited using waveform "A." These images originally appeared in Ref. 48. Global Mn content of each alloy is shown in the upper left corner of each panel.
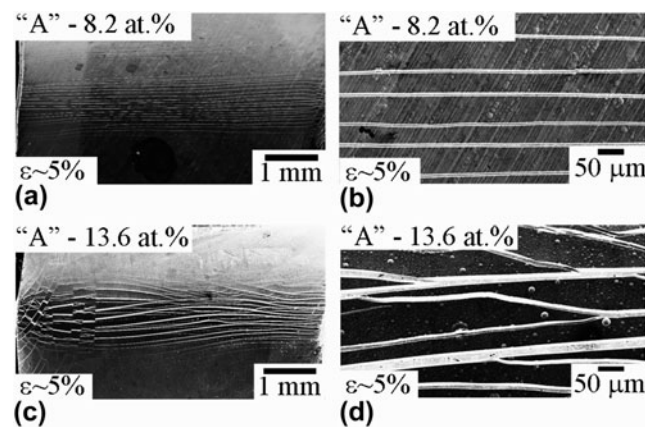

FIG. 2. SEM images of the convex bent surfaces of the "A" 8.2 and 13.6 at.% Mn alloys upon application of ~5% tensile strain are shown in (a)-(b) and (c)-(d), respectively. The relatively straight crack paths are characteristic of brittle fracture.

pinning and accumulation,[13,14] it is also plausible that these extremely fine grains impair the alloy's ability to deform plastically.

IV. DUCTILIZATION OF Al–Mn ELECTRODEPOSITS

As discussed in the previous section, our work on DC deposited Al–Mn alloys suggested that a controlling factor in the development of nanostructure is the kinetics at the cathode. This observation provides a motivation for the introduction of PC into the deposition process because it can significantly affect the kinetic processes on the electrode and thereby affect nanostructure formation. For example, in other alloy systems (generally using aqueous baths), waveforms with "off-time" have been found to affect aspects of the deposits such as chemical composition[32,49–51] and homogeneity,[49] surface roughness,[49,52,53] grain size distribution,[47,51,52,54,55] and texture.[50] Reverse pulse waveforms have also been found to significantly affect such coating attributes.[23,52,56–59] In the case of alloy coatings in particular, periodic anodic pulses can be used to selectively remove the element with the highest oxidation potential, thus allowing an additional degree of control over the alloy composition.

In this section, we explore the possible utility of PC deposition to improve the nanostructure and properties of Al–Mn electrodeposits. We consider square waveforms, comprising segments defined by their current densities (e.g., "i_1" and "i_2") and time duration (e.g., "t_1" and "t_2"). We use positive numerical values of i to denote a cathodic current (i.e., current that flows in such a direction as to reduce metal ions into atoms on the cathode surface). Table I summarizes the waveforms used. Briefly, these can be grouped into three series of experiments focused on the exploration of a single processing variable each:

(i) Series I: Current amplitude. To systematically explore the role of current amplitude at a fixed set of pulse durations and in a fixed bath composition, we set the first pulse current density at $i_1 = 6$ mA/cm^2 and the pulse durations at $t_1 = t_2 = 20$ ms and vary the second current density, i_2. This series of experiments is captured by waveforms "A"–"F" in Table I. Note that waveforms "A"–"C" contain cathodic pulses only and that waveform "A" is simply a DC current, identical to the one used in Ref. 48 and in the previous section. Waveform "D" represents classical pulse plating with an "off-time" pulse period in which no current flows. Waveforms "E"–"F" comprise anodic pulses, during which current flows such that atoms are selectively removed from the growing film. For this series, the bath composition was fixed at 0.08 mol/L MnCl$_2$.

(ii) Series II: Pulse durations. To investigate the effects of pulse duration at a fixed set of pulse current densities and in a fixed bath composition, we fix the current densities at $i_1 = 6$ mA/cm^2, $i_2 = -3$ mA/cm^2, and the first pulse durations at $t_1 = 20$ ms and vary the second pulse duration, t_2. This series of experiments is captured by waveforms "A," "G," "H," and "E" in Table I, where the anodic pulse duration increases from 0 to 20 ms at increments of 5 ms. For this series, the bath composition was also fixed at 0.08 mol/L MnCl$_2$.

(iii) Series III: Bath composition. To investigate the effects of bath composition for a single fixed PC waveform, we performed a series of experiments in 11 different baths comprising different Mn contents, all using waveform "E." The bath compositions ranged from 0 to 0.17 mol/L MnCl$_2$ and the resulting alloy compositions range from 0 to ~14 at.% Mn.

The experiments and results presented in this section are intended primarily as an initial parametric study on the effect of PC plating on the key properties of Al–Mn alloys, namely film ductility and in selected cases, hardness. In the subsections that follow, we therefore present the results without delving deeply into the potential causes for the reported trends. In a later section, we will provide more detailed scientific investigation on possible mechanisms for the observations in this section.

A. Effects of pulse current density, i_2

To investigate the effects of varying the current density i_2, we compare results obtained using waveforms "A"–"F." Interestingly, EDX measurements of alloys deposited using these waveforms in solutions containing 0.08 mol/L MnCl$_2$ all contain ~8 at.% Mn, thus indicating that i_2 has negligible effects on the alloy composition, at least to within experimental uncertainties in composition measurements and for the current set of fixed processing parameters.

Guided bend tests were carried out on these alloys and images of the strained surfaces are presented in Fig. 3. Images in the left and right columns correspond to alloys that were strained to ~37 and ~13%, respectively. Images on the same row belong to alloys that were produced by the same current waveform. The current density i_2 decreases from positive to negative from the topmost to bottommost row.

Briefly, we observe that the vast majority of the tested samples still exhibit fracture under the test conditions used here. More specifically, at a large applied strain of 37%, all these alloys exhibited extensive cracking, suggesting failure well below this strain level. Interestingly, though, as seen in the left column of Fig. 3, decreasing the magnitude of i_2 changes the character of the cracking in a significant way; whereas the "A" alloys cracked across the full sample widths, those produced by most other waveforms did not. For positive values of i_2 (i.e., waveforms "A"–"C"), decreasing the magnitude of the positive pulse current causes the cracks to become more distributed; finer cracks of higher number density are produced in the
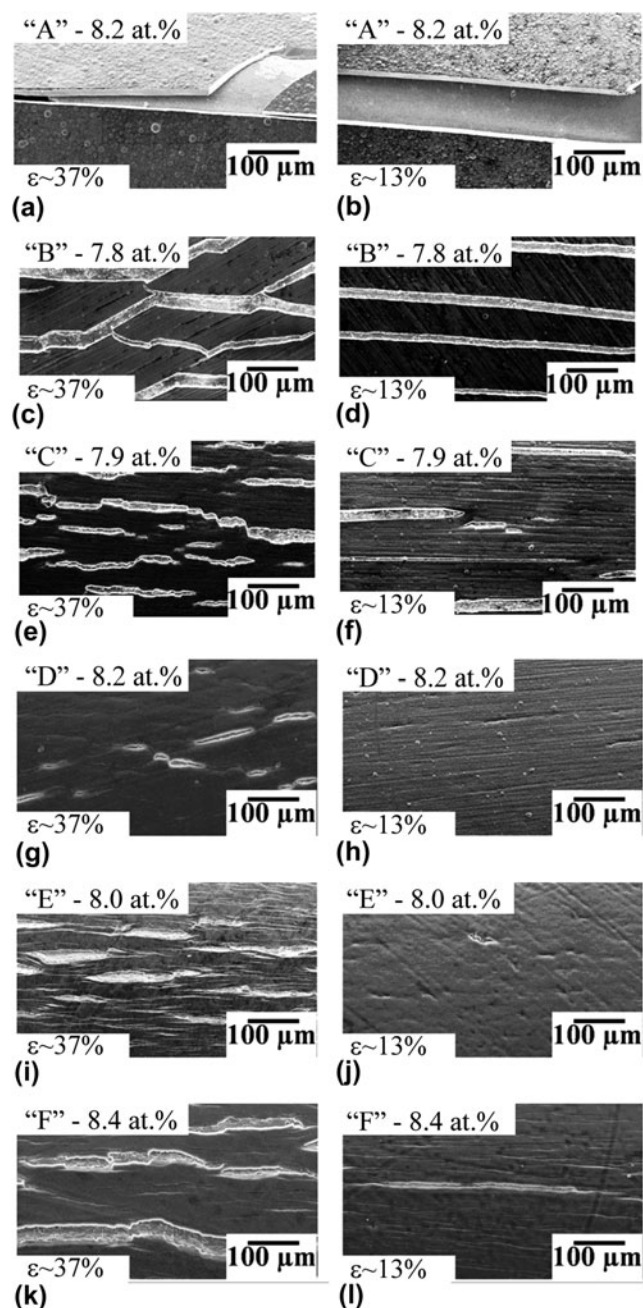
FIG. 3. SEM images of bent surfaces of ~8 at.% Mn alloys produced by different waveforms. Images on the left column correspond to samples that were strained to ~37%. Images on the right correspond to samples that were bent strained to ~13% true strain. i_2 decreases from +6 mA/cm^2 to −3.75 mA/cm^2 from the topmost to bottommost row. The letters denote the waveform used; see Table I.

PC samples, and no cracks propagating across the full width of the "C" alloy could be found. This trend seems to reverse for the "D," "E," and "F" alloys, as i_2 becomes more negative and the cracks again become larger and more contiguous.

A similar trend in the fracture behavior is reflected in the samples strained only to 13%. As we traverse through the sequence "A"–"F" in the right column of Fig. 3, we see first an increase in the degree of distribution of the

fractures and then a subsequent decrease. The important difference at 13% strain as compared to 37% is that around the inflection point in this trend, no cracks are observed at all; films "D" and "E" are apparently ductile at the lower strain of 13%. Since all these alloys exhibit about the same composition, it is a noteworthy result that their fracture properties can be so significantly changed, from decisively brittle to apparently ductile, with merely a change in the shape of the applied current waveform during processing. This is a theme that we will return to discuss at greater length later. For the moment, it is especially interesting that there is an apparent optimum in the range of $i_2 = 0$ to −3 mA/cm^2 where the most significant increase in film ductility is observed. Therefore, in the following subsection, we fix $i_2 = -3$ mA/cm^2 in this preferred range and investigate the effects of varying the pulse duration, t_2.

B. Effects of pulse duration, t_2

To investigate the effects of varying the pulse duration t_2, we compare results obtained using waveforms "A," "G," "H," and "E." Waveform "A" corresponds to DC plating with $t_2 = 0$, while the other three waveforms are all reverse pulse waveforms with increasing reverse pulse duration. Note that sample "E" is the same one described in the previous section, near the apparent peak in ductility among the various waveforms studied there. EDX measurements of alloys deposited using all four of these waveforms in solutions containing 0.08 mol/L MnCl$_2$ all contain ~8 at.% Mn, thus indicating that t_2 has negligible effects on the alloy composition (to within experimental uncertainties in composition measurements).

Guided bend tests were carried out on these alloys and images of the strained surfaces are presented in Fig. 4. The pulse duration t_2 increases from the topmost to bottommost row. It is useful to begin with a discussion of the endpoints of this series, i.e., samples "A" and "E," both of which were included in the data set in the previous section. The DC "A" sample is very brittle [Fig. 4(a) and 4(b)], while the "E" sample (with $t_2 = 20$ ms) is apparently ductile at 13% strain [Fig. 4(h)].

Interestingly, the series between these extremes shows a trend of gradual ductilization; increasing the pulse duration t_2 leads to an increase in crack distribution. Whereas the "A" and "G" alloys ($t_2 = 0$ and 5 ms, respectively) exhibit cracks that propagate across the full sample width at both applied tensile strains levels of ~37 and ~13%, the "H" and "E" alloys did not crack across the entire width. And, as noted earlier, sample "E" is apparently ductile at a strain of ~13%. These results thus suggest that a sufficiently long anodic pulse is apparently needed to achieve significant ductility.

C. Effects of bath composition

To investigate the effects of bath composition for a single fixed PC waveform, we performed a series of
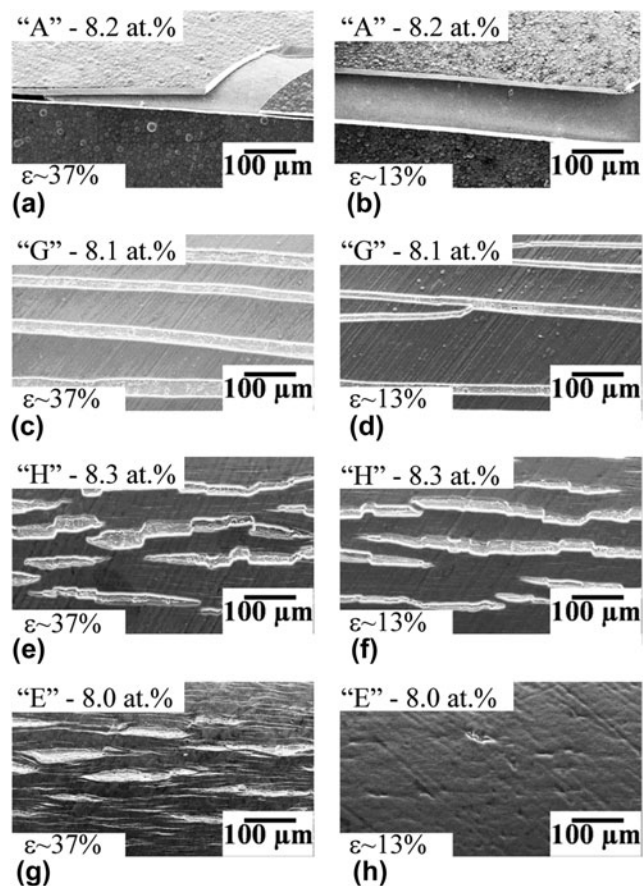
FIG. 4. SEM images of bent surfaces of ~8 at.% Mn alloys produced by waveforms with different t_2. Images on the left column correspond to samples that were strained to ~37%. Images on the right correspond to samples that were subject to a tensile strain of ~13%. The pulse duration t_2 increases from 0 to 20 ms from the topmost to bottommost row. The letters denote the waveform used; see Table I.

FIG. 5. SEM images of the bent surfaces of the "E" alloys after guided bend tests, where the applied strain was ~37%.

electrodeposition experiments in several different baths comprising different Mn contents, all using waveform "E." This series of experiments resulted in alloys with compositions ranging from 0 to 13.6 at.% Mn, so we label the samples from this series of experiments as "E-x," where x denotes their atomic concentration of Mn. Figure 5 assembles images of the strained surfaces of the "E" alloys after the guided bend test with an applied strain of ~37%.

Figure 5(a)–5(e) shows that the strained surfaces of "E" alloys with Mn contents up to 7.8 at.%. These images reveal a significant change in the surface topography, which correlates to a change in internal structure as the Mn content rises; this will be explored in more detail in a later section. For the moment, we concentrate on the other phenomenon revealed by these images, namely, none of the samples E-0 through E-7.8 exhibit any cracks despite being strained to 37% in tension; these alloys are all apparently ductile to large strains. On the other hand, the same level of strain resulted in micron-sized fissures with rough edges in the E-8.2 alloy, as shown in Fig. 5(f). The severity of cracking
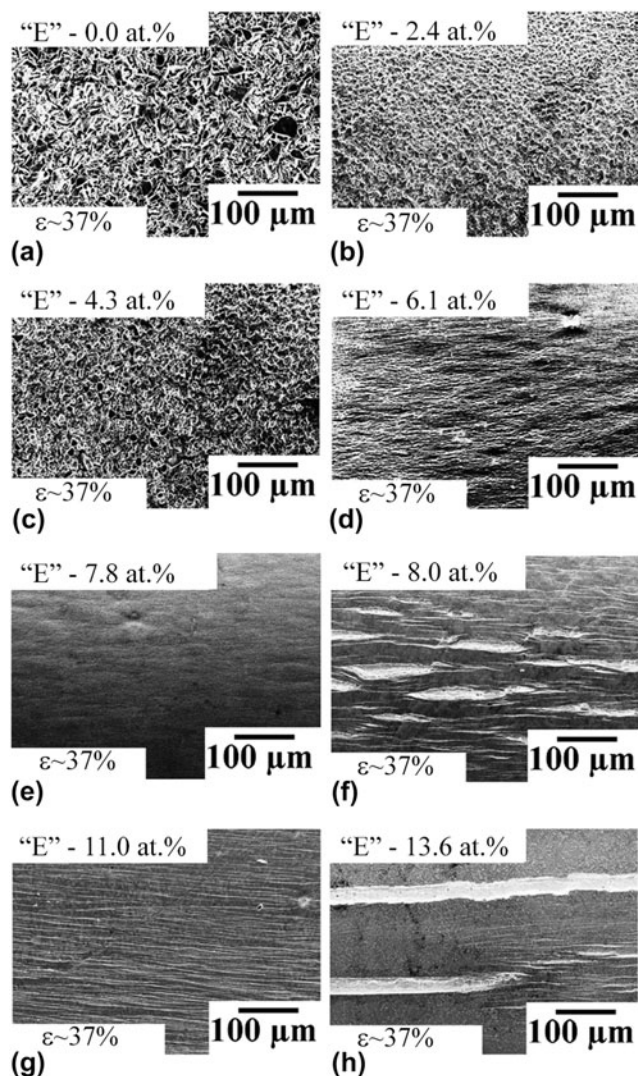
increased further as the Mn content increased to 13.6 at.%, where large cracks spanning a large fraction of the sample width were observed, as shown in Fig. 5(h). Thus, Fig. 5 suggests that the pulse current "E" alloys containing up to ~7.8 at.% Mn exhibit excellent film ductility (>37%), but this is compromised at higher Mn contents.

To further quantify the tensile ductility of "E" alloys with higher Mn contents, additional bend tests were performed on samples containing 8.0 and 13.6 at.% Mn, where the applied strains were gradually lowered from 37%. It was found that reduction of the applied strain to ~13 and ~5% resulted in crack-free surfaces for the 8.2 and 13.8 at.% Mn specimens, respectively.

The hardness of the "E" alloys was assessed by nanoindentation and microindentation experiments, with results shown in Fig. 6. As the Mn content increases, the hardness generally increases. Such an increase in hardness may be

attributed to a combination of solid solution strengthening and microstructural refinement, which will be discussed in a later section.

D. Fractography of PC alloys

In the previous subsections, we presented guided bend test results indicating that alloys electrodeposited with PC waveforms exhibit better film ductility than their DC counterparts. Some of the more exemplary results include those for the E-7.8 and E-8.2 alloys, with film ductilities of at least ~37 and ~13%, respectively. To support the interpretation of these results as indicative of legitimate plasticity, it is useful to examine the fracture surfaces of these two alloys.

The fracture surfaces of the E-7.8 and E-8.2 alloys are presented in Fig. 7(a) and 7(b), respectively. In these images, black solid lines are used to demarcate the boundary between the Al–Mn film and copper substrate. Chisel-type or knife-edge rupture is observed in both samples, with an apparent reduction in area of almost 100%. Since such chisel-type fracture is characteristic of ductile materials when void development and coalescence are suppressed,[60,61] we interpret the images in Fig. 7(a) and 7(b) as consistent with the

reported high film ductility we measured in the previous sections.

The double-headed arrows in Fig. 7 represent rough approximations of the film thicknesses at the trailing regions of the rupture, i.e., outside of the neck zone. Making such measurements across the entire sample gives average film thickness values in the plastically deformed (unnecked) zone of ~7 and ~9 μm for the 7.8 and 8.2 at.% Mn films, respectively, and these in turn correspond to reductions of 42 and 25% from the initial film thicknesses before testing. These values agree in general with the quantitative film ductility values for these alloys (37 and 13%, respectively). Thus, the results presented in Fig. 7 provide corroborating evidence that legitimate plastic flow can occur in these PC alloys and also qualitatively illustrate the decreasing trend in toughness as solute content increases, consistent with the bend test results presented in Sec. IV. C.

V. EFFECTS OF PC DEPOSITION ON STRUCTURE AND PROPERTIES

The film ductility test results presented in the previous section show that pulse waveforms improve the film ductility of Al–Mn electrodeposits over those prepared using conventional DC deposition. Our results show that "off-time" and mild anodic pulses favor ductility, as do longer anodic pulse durations; among the samples tested, the "D" and "E" waveforms seemed to deliver the greatest benefit. More importantly, the data presented above show that pulse parameters afford a relatively easy and convenient route to tune and optimize the film ductility of electrodeposited Al–Mn alloys, without dramatically changing their composition or hardness. This is of course of practical interest, but it also raises a scientific question as to what structural differences are induced by PC, which lead to this ductilization. In this section, we investigate the effects of pulsing on alloy structure and seek to understand and relate the differences in structure between the PC and DC alloys to their dramatically different film ductilities. To this end, alloys produced using the "A" (DC) and "E" (PC) waveforms will be compared in detail, and we will again use the notation "A-x" and "E-x" to denote combinations of waveform and atomic composition.

FIG. 6. Plot summarizing the hardness values of the "E" alloys obtained using nanoindentation and microindentation.

A. Alloy composition

Figure 8 summarizes the effects of electrolyte composition and current waveform on the Mn content of the as-deposited alloys. Over most of this range, it is very interesting to observe that waveforms "A" and "E" both tend to deliver samples of essentially identical composition. It is only for alloys electrodeposited in electrolytes that contain between ~0.1 and 0.15 mol/L of $MnCl_2$, that there is any measurable difference: alloys produced by waveform "E" have somewhat lower Mn content than the
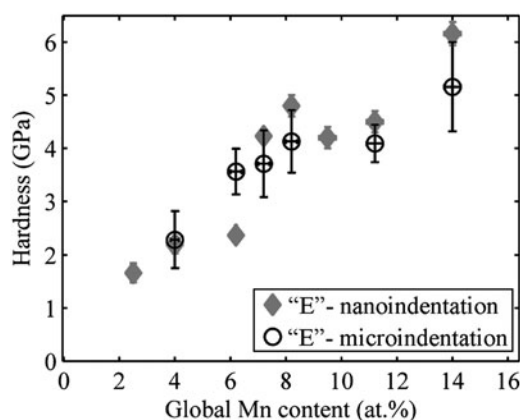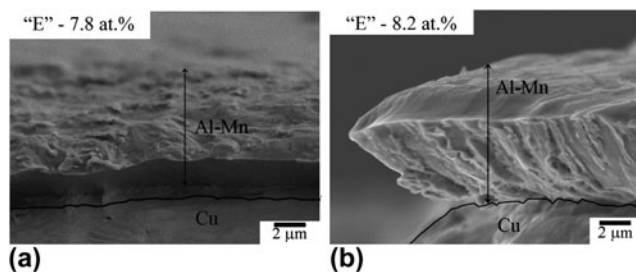

FIG. 7. SEM images of the fracture surfaces of "E" alloys containing (a) 7.8 at.% Mn and (b) 8.2 at.% Mn. The solid black lines demarcate the interface between the Al–Mn film and copper substrate, and the double-headed arrows indicate the film thickness in the trailing regions behind the rupture.

DC "A" alloys. We infer that within this range of electrolyte composition, the anodic pulse preferentially removes Mn from the as-deposited alloy. Interestingly, as shown in Fig. 8, the corresponding alloy compositions lie between ~8 and ~14 at.% Mn. Recall that for the "A" alloys, Mn content of ~8 at.% corresponds to the onset of a duplex structure, where nanocrystalline grains coexist with an amorphous phase, and ~14 at.% coincides with the disappearance of the crystalline phase (see Table II and Fig. 1). Therefore, the results presented in Fig. 8 suggest that anodic pulses exert the most influence on composition in the very range of compositions where the structure is transitioning through the nanoscale regime. In the following subsections, we will cross-compare the structure and properties of alloys with similar Mn contents deposited using waveforms "A" and "E," with more emphasis placed on alloys with Mn contents around and above ~8 at.%.

B. Surface morphology

Figure 9 assembles the surface morphologies of the as-deposited alloys. Images on the left column correspond to the DC "A" alloys, which were originally presented in Ref. 48, while images on the right correspond to the PC "E" alloys. Images of alloys with similar Mn content are placed on the same row. Note that images of the "A" alloys (left column) are half as magnified as those of the "E" alloys (right column).

The surface morphologies of the "A" alloys show an abrupt transition from highly angular/facetted structures [images (a) and (c)] to rounded nodules [images (e), (g), and (i)] at ~8 at.%. The surface morphologies of the "E" alloys, on the other hand, show a gradual transition from angular and smaller structures in images (b) and (d), to a smooth and almost featureless surface in image (f), before rounded nodules start to appear in images (h) and (j). As discussed in Ref. 48, the dramatic transition from pyramidal to nodular structures in the "A" alloys is a signature
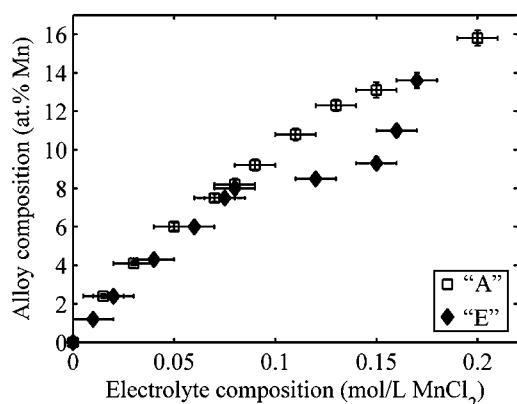
of an abrupt microcrystalline-to-nanocrystalline structural transition,[59] which is evidenced in more detail by the TEM observations of the "A" alloys in Fig. 1. That the surface morphologies of the "E" alloys exhibit a much more subtle reduction in surface feature size over the same range of compositions suggests a more gradual structural change; this will be explored in greater detail in the following subsections.

C. Grain size and phase distribution

Figure 10 shows TEM images along with the electron diffraction patterns of the "E" alloys; those of the "A"
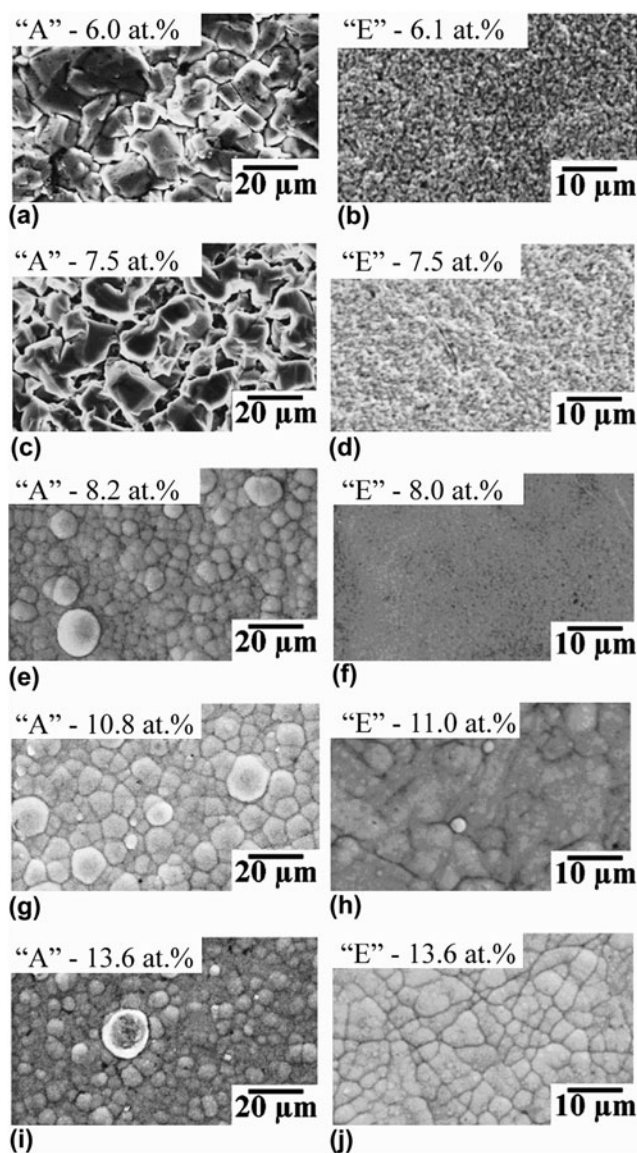

FIG. 9. Surface morphologies of alloys electrodeposited using waveform "A" (left column) and waveform "E" (right column). Images on same row have similar Mn content. Note that magnification of images on the left column is half that of those on the right. The images in the left column originally appeared in Ref. 48.

FIG. 8. Plot showing the effects of varying electrolytic composition on the Mn content of the alloys electrodeposited using waveforms "A" and "E."

alloys were presented earlier in Fig. 1 for comparison. The phase content, as inferred from the electron diffraction patterns in Fig. 10 (and confirmed by x-ray diffraction experiments not shown here), follows a pattern with respect to solute content: alloys with up to 7.8 at.% Mn comprise a single FCC phase; alloys with Mn contents between 8.2 and 10.4 at.% contain an amorphous phase coexisting with the FCC phase, as evidenced by the diffuse halo between the (111) and (200) FCC rings; alloys with more than 11 at.% Mn consist of a single amorphous phase.

In broad strokes, the sequence of structures observed in the PC "E" alloys is generally similar to that seen in the DC "A" alloys earlier. However, there are subtle but significant details that differ between them. For example, the composition range over which the alloys clearly exhibit a two-phase structure is apparently somewhat narrower for the "E" alloys (which is apparently fully amorphous by 11 at.% Mn) than that of the "A" ones (which remains two-phase up to 12.3 at.% Mn). The dramatic change in phase content within such a narrow range of solute composition of the "E" alloys was verified through a separate study using atom probe tomography.[62]

The emergence of nanostructure (reduction in grain size) as a function of alloying addition is also different between these alloy series, as evidenced in the bright-field images in Figs. 1 and 10. Figure 10(a) and 10(b) shows that "E" alloys with 7.0 and 7.8 at.% Mn contents exhibit nanometer-sized grains, with averages of ~500 and ~160 nm, respectively. Further increase in Mn contents from 8.2 to 10.4 at.% causes the average grain size to decrease to ~37 and ~5 nm, as shown in Fig. 10(c)–10(e). What is interesting about this reduction in grain size is that it is rather gradual and without obvious discontinuities; the FCC Al(Mn) phase simply refines until it reaches the nanometer range, whereupon it gradually surrenders volume fraction to the competing amorphous phase. This is in stark contrast to the DC "A" alloys in Fig. 1, which retain large grain sizes (>7 μm) until the competing amorphous phase emerges and concomitantly induces fine nanoscale FCC grains [Fig. 1(a) and 1(b)].

This critical difference between DC "A" and PC "E" alloys can best be appreciated graphically, as illustrated in Fig. 11(a), where the region shaded gray corresponds to the composition range where the alloys exhibit a single crystalline phase. Whereas the "A" alloys show an abrupt microcrystalline-to-nano/duplex transition upon the appearance of an amorphous phase at ~8 at.% Mn, the grain size of the "E" alloys gradually decreases from microns to nanometers at ~7 at.% Mn, before an amorphous phase emerges at ~8 at.% Mn. We conclude that pulse current waveform promotes grain refinement but also somewhat opposes the formation of the competing amorphous phase. An important outcome of this is that in the PC alloys, it is possible to synthesize single-phase nanocrystalline FCC alloys, whereas in the DC alloys it is not; from Fig. 11(a), the region in which this is possible is about ~6–8 at.% Mn. Single-phase alloys in this range offer the promise of high strength and hardness due to Hall–Petch strengthening, while the lack of amorphous phase is anticipated to be beneficial for ductility or toughness.
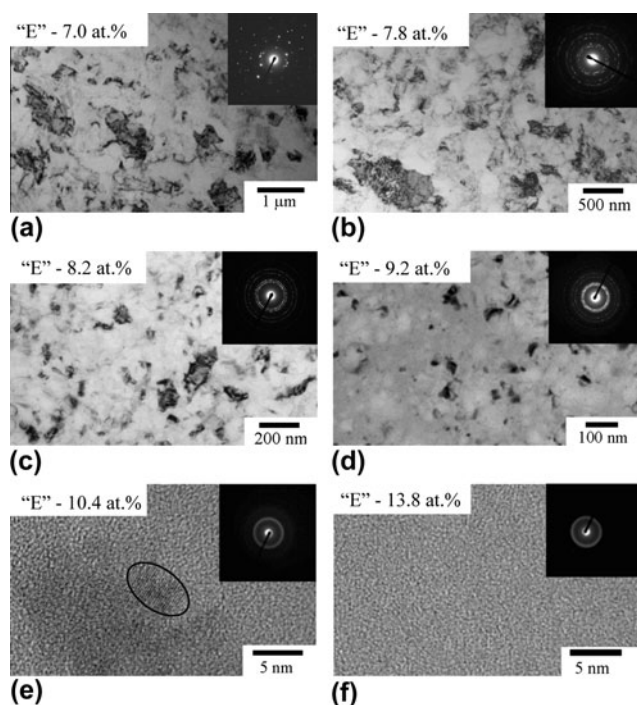

FIG. 10. Bright-field TEM images and electron diffraction patterns of the "E" alloys. Note the single-phase nanocrystalline structures in (a) and (b). Images (c)-(e) show that the two-phase alloys no longer comprise the domain network structures observed in the "A" alloys (cf. Fig. 1).
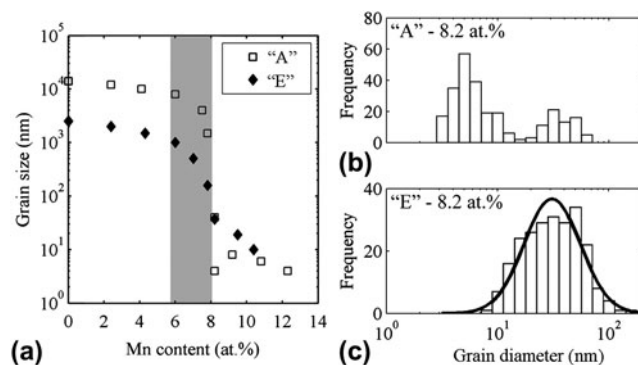

FIG. 11. (a) Average grain sizes of "A" and "E" alloys at different Mn compositions. Region shaded gray represents the composition range within which the "E" alloys contain a single FCC phase with submicrometer grain sizes. The grain size distribution of ~250 grains observed in the 8.2 at.% Mn alloys are shown in (b) for the "A" alloy and (c) for the "E" alloy. Also shown in (c) is a lognormal distribution curve.

To underscore the unique nanostructure achievable in the PC specimens, we analyze in detail the grain size distribution of ~250 grains observed in the "A" and "E" alloys containing 8.2 at.% Mn in Fig. 11(b) and 11(c), respectively. The thick solid line in Fig. 11(c) represents a lognormal distribution curve. In contrast to the DC "A" alloy, which exhibits a bimodal grain size distribution centered at ~40 and ~3 nm, that of the PC "E" alloy matches well with the lognormal distribution with an average grain size of ~37 nm. In addition to changing the grain size distribution, the TEM images presented in Fig. 10(c)–10(e) show that the two-phase "E" alloys do not exhibit the characteristic duplex domain network structure that was observed in the "A" alloys [cf. Fig. 1(b)–1(e)]. Instead, the structure appears like a conventional uniform nanostructured material.

D. Postmortem TEM

The above examinations of "A" and "E" alloys suggest that the PC "E" alloys exhibit special structures that are not obtained under DC processing conditions. Specifically, it seems that PC permits uniform nanostructured Al–Mn with grain sizes below 100 nm, without significant amorphous phase content. It is interesting that the alloys which fall in this range (e.g., E-7.8) are also the ones with the highest measured film ductilities. We infer from this that the uniform nanostructure in these PC alloys is, in fact, the reason why they exhibit large ductilities where other alloys do not. A better appreciation of why this might be the case is provided by postmortem TEM exploration of deformed samples. An image of an E-7.8 alloy that sustained a tensile strain of ~37% without cracking are shown in Fig. 12(a) and 12(b), where (a) corresponds to a region far away from the bend and (b) corresponds to a strained/bent region. This specimen is single-phase FCC and has a grain size of ~160 nm.

A comparison of the bright-field images in Fig. 12(a) and 12(b) reveals a significant difference between the unstrained and strained volumes: straining is associated with noticeable grain growth. This is observed easily by eye in the bright-field images, and the corresponding electron diffraction pattern in Fig. 12(b) also comprises larger and more discrete spots than that of the as-deposited sample [Fig. 12(a)] under identical diffraction conditions. The deformed grain structure also seems to exhibit characteristics of abnormal grain growth, with a small population of very large grains that have grown quickly.

Deformation-induced grain growth has been extensively observed in other nanocrystalline materials[63–67] and has been associated with grain boundary sliding,[63] grain rotation and coalescence,[64,65] and stress-assisted grain boundary migration.[66,67] Notably, prior work on pure nanocrystalline Al with grain sizes in a similar range to the present E-7.8 sample (~160 nm) have shown similar deformation-induced grain growth. Not only is the occurrence of this
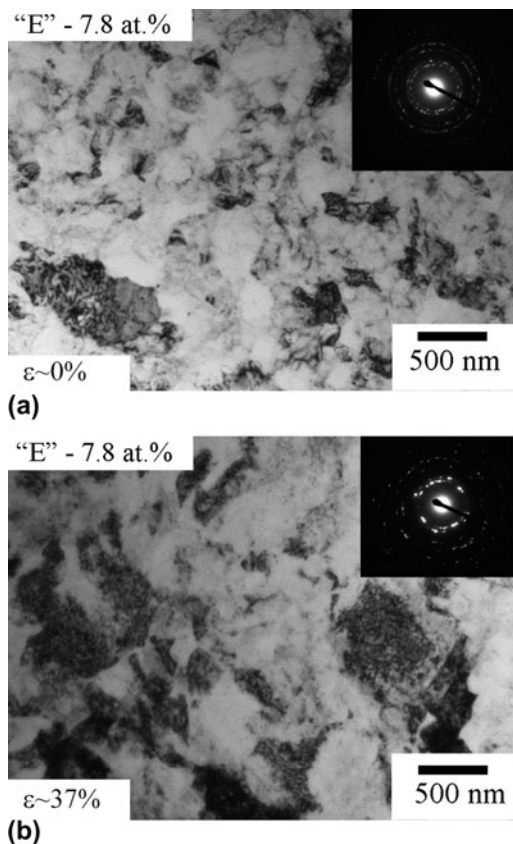

FIG. 12. TEM images of a 7.8 at.% Mn alloy produced using waveform "E"; image (a) belongs to a region far from the bend; image (b) corresponds to a bent region where the applied tensile strain is ~37%.

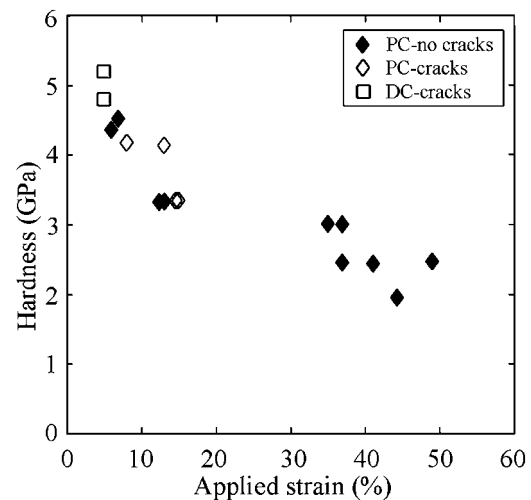FIG. 13. Plot showing hardness versus applied tensile strain of our electrodeposited Al–Mn alloys. Samples produced using PC waveform and did not exhibit any cracks after the guided bend test are represented by solid black diamonds. PC samples that failed, i.e., exhibited fissures or cracks of any length and width, are denoted by white diamonds. Failed DC samples are represented by white squares.

phenomenon associated with increased plastic straining in tension by itself, but additionally, detailed characterization studies have indicated that the increase in grain size can subsequently trigger the activation of more conventional deformation mechanisms, such as intragranular dislocation multiplication and accumulation, which also promote strain hardening, toughness, and large plastic strains.[67–69] Our postmortem TEM results in Fig. 12 are broadly consistent with these prior observations, and on this basis, it seems plausible that the increased ductility we achieve in these alloys is a result of their fine uniform structures being capable of stress- and/or strain-induced grain growth. We propose that the main advantage of PC over DC processing may be the development of uniform nanostructures with regular grain structures, as compared to the more complex dual-phase nanostructures that DC processing produces (cf. Fig. 11).

VI. CONCLUSION

In this study, we used both DC and a variety of PC waveforms to electrodeposit Al–Mn alloys. Screening various PC waveforms for their effect on film ductility, we found that "off-time" and anodic pulses applied during deposition improve film ductility, as do longer anodic pulse durations. This study shows that pulse parameters afford a relatively easy and convenient route to tune and optimize the ductility of electrodeposited Al–Mn alloys, without significantly changing the composition or hardness. The use of PC current does, on the other hand, affect the grain size and homogeneity of the nanostructure in the deposits, as studied through TEM observations.

Figure 13 summarizes the hardness and film ductility of our DC and PC alloys. The open symbols show samples that cracked during testing to the denoted applied strain, and solid symbols represent samples that did not exhibit any crack or fissure after the guided bend tests. The results in Fig. 13 summarize our finding that whereas the DC nanostructured and amorphous alloys exhibit high hardnesses, they are extremely brittle. We attribute the apparent brittleness in the DC alloys to (i) concomitant appearance of a brittle amorphous phase upon grain size refinement into the nanometer regime, (ii) a large fraction of grains that are less than ~10 nm in the nanostructured alloys, and (iii) inhomogeneous phase distribution.

In contrast, the PC alloys are found to exhibit a good combination of high hardness and film ductility. PC processing leads to a number of structural advantages that apparently ductilize the Al–Mn alloys: (i) grain refinement to the nanocrystalline range without the introduction of a competing amorphous phase, (ii) unimodal nanocrystalline grain size distribution, and (iii) more homogeneous structure. The significant increase in apparent ductility in the PC alloys was studied through postmortem TEM observations of an exemplary Al-7.8 at% Mn alloy after straining in

tension to 37%. In the strained region, significant grain growth was observed as compared to an unstrained region of the same sample. In line with prior literature on deformation-induced grain growth in other nanocrystalline materials, this observation offers a plausible explanation for the observed ductilization trend, as grain growth during straining not only provides a mechanism to sustain plastic flow without fracture, but also can trigger classical deformation mechanisms (i.e., intragranular dislocation plasticity) in the coarsened grains.

These results highlight the critical value of processing technologies that permit subtle tuning of the nanostructure in alloys. With a fine degree of control over the structure of Al–Mn by PC electrodeposition, new combinations of high strength, high toughness, and low density may be achievable in these alloys.

ACKNOWLEDGMENTS

REFERENCES

1. A. Inoue: Amorphous, nanoquasicrystalline and nanocrystalline alloys in Al-based systems. *Prog. Mater. Sci.* **43**, 365 (1998).
2. K.M. Youssef, R.O. Scattergood, K.L. Murty, and C.C. Koch: Nanocrystalline Al-Mg alloy with ultrahigh strength and good ductility. *Scr. Mater.* **54**, 251 (2006).
3. P.V. Liddicoat, L. Xiao-Zhou, Z. Yonghao, Z. Yuntian, M.Y. Murashkin, E.J. Lavernia, R.Z. Valiev, and S.P. Ringer: Nanostructural hierarchy increases the strength of aluminium alloys. *Nat. Commun.* **1**(63), 1–7 (2010).
4. Y. Kawamura, H. Mano, and A. Inoue: Nanocrystalline aluminum bulk alloys with a high strength of 1420 MPa produced by the consolidation of amorphous powders. *Scr. Mater.* **44**, 1599 (2001).
5. T. Topping, B. Ahn, Y. Li, S. Nutt, and E. Lavernia: Influence of process parameters on the mechanical behavior of an ultrafine-grained Al alloy. *Metall. Mater. Trans. A* **43**, 505 (2012).
6. B. Ahn, R. Mitra, E.J. Lavernia, and S.R. Nutt: Effect of grain size on strain rate sensitivity of cryomilled Al-Mg alloy. *J. Mater. Sci.* **45**, 4790 (2010).
7. Y. Li, Y.H. Zhao, V. Ortalan, W. Liu, Z.H. Zhang, R.G. Vogt, N.D. Browning, E.J. Lavernia, and J.M. Schoenung: Investigation of aluminum-based nanocomposites with ultra-high strength. *Mater. Sci. Eng. A* **527**, 305 (2009).
8. T.T. Sasaki, T. Ohkubo, and K. Hono: Microstructure and mechanical properties of bulk nanocrystalline Al-Fe alloy processed by mechanical alloying and spark plasma sintering. *Acta Mater.* **57**, 3529 (2009).
9. B.J. Yang, J.H. Yao, J. Zhang, H.W. Yang, J.Q. Wang, and E. Ma: Al-rich bulk metallic glasses with plasticity and ultrahigh specific strength. *Scr. Mater.* **61**, 423 (2009).
10. Y.H. Zhao, X.Z. Liao, S. Cheng, E. Ma, and Y.T. Zhu: Simultaneously increasing the ductility and strength of nanostructured alloys. *Adv. Mater.* **18**, 2280 (2006).
11. Y.T. Zhu and T.G. Langdon: The fundamentals of nanostructured materials processed by severe plastic deformation. *JOM* **56**, 58 (2004).

12. E. Ma: Eight routes to improve the tensile ductility of bulk nanostructured metals and alloys. *JOM* **58**, 49 (2006).

13. J. Schiotz, F.D. Di Tolla, and K.W. Jacobsen: Softening of nanocrystalline metals at very small grain sizes. *Nature* **391**, 561 (1998).

14. T.G. Nieh and J. Wadsworth: Hall-Petch relation in nanocrystalline solids. *Scr. Metall. Mater.* **25**, 955 (1991).

15. H. Gleiter: Nanocrystalline materials. *Prog. Mater. Sci.* **33**, 223 (1989).

16. W. Laslouni, K. Taibi, D. Dahmoun, and M. Azzaz: Structure and properties of nanocrystalline $Cu_{70}Fe_{18}Co_{12}$ obtained by mechanical alloying. *J. Non-Cryst. Solids* **353**, 2090 (2007).

17. J.J. Sunol, A. Gonzalez, J. Bonastre, M.T. Clavaguera-Mora, and B. Arcondo: Synthesis and characterization of nanocrystalline FeNiZrB developed by mechanical alloying. *J. Alloys Compd.* **434**, 415 (2007).

18. E. Hellstern, H.J. Fecht, Z. Fu, and W.L. Johnson: Structural and thermodynamic properties of heavily mechanically deformed Ru and AlRu. *J. Appl. Phys.* **65**, 305 (1989).

19. M. Stueber, H. Holleck, H. Leiste, K. Seemann, S. Ulrich, and C. Ziebert: Concepts for the design of advanced nanoscale PVD multilayer protective thin films. *J. Alloys Compd.* **483**, 321 (2009).

20. R.Z. Valiev, R.K. Islamgaliev, and I.V. Alexandrov: Bulk nanostructured materials from severe plastic deformation. *Prog. Mater. Sci.* **45**, 103 (2000).

21. H. Hahn: Gas phase synthesis of nanocrystalline materials. *Nanostruct. Mater.* **9**, 3 (1997).

22. H. Hahn and R.S. Averback: The production of nanocrystalline powders by magnetron sputtering. *J. Appl. Phys.* **67**, 1113 (1990).

23. A.J. Detor and C.A. Schuh: Tailoring and patterning the grain size of nanocrystalline alloys. *Acta Mater.* **55**, 371 (2007).

24. K.R. Sriraman, S.G.S. Raman, and S.K. Seshadri: Corrosion behaviour of electrodeposited nanocrystalline Ni-W and Ni-Fe-W alloys. *Mater. Sci. Eng. A* **460**, 39 (2007).

25. B.Y.C. Wu, P.J. Ferreira, C.A. Schuh, and T.G. Nieh: Nanostructured Ni-Co alloys with tailorable grain size and twin density. *Metall. Mater. Trans. A* **36A**, 1927 (2005).

26. F. Ebrahimi, G.R. Bourne, M.S. Kelly, and T.E. Matthews: Mechanical properties of nanocrystalline nickel produced by electrodeposition. *Nanostruct. Mater.* **11**, 343 (1999).

27. F. Ebrahimi, D. Kong, T.E. Matthews, and Q. Zhai: Processing of metallic nanostructures by electrodeposition techniques, in *Processing and Fabrication of Advanced Materials VII*, edited by T.S. Srivastan and K.A. Khor (TMS Publication, Warrendale, PA, 1998), p. 509.

28. U. Erb: Electrodeposited nanocrystals: Synthesis, properties and industrial applications. *Nanostruct. Mater.* **6**, 533 (1995).

29. H. Natter and R. Hempelmann: Tailor-made nanomaterials designed by electrochemical methods. *Electrochim. Acta* **49**, 51 (2003).

30. K. Boylan, D. Ostrander, U. Erb, G. Palumbo, and K.T. Aust: In-situ TEM study of the thermal stability of nanocrystalline Ni-P. *Scr. Metall. Mater.* **25**, 2711 (1991).

31. A.R. Jones, J. Hamann, A.C. Lund, and C.A. Schuh: Nanocrystalline Ni-W alloy coating for engineering applications. *Plat. Surf. Finish.* **97**, 52 (2010).

32. H. Natter, M. Schmelzer, and R. Hempelmann: Nanocrystalline nickel and nickel-copper alloys: Synthesis, characterization, and thermal stability. *J. Mater. Res.* **13**, 1186 (1998).

33. M.R. Carl: Electroforming. *Met. Finish.* **93**, 369 (1995).

34. T. Hart and A. Watson: Electroforming. *Met. Finish.* **100**, 372 (2002).

35. B. Grushko and G.R. Stafford: Structural study of electrodeposited aluminum-manganese alloys. *Metall. Trans. A* **20**, 1351 (1989).

36. H.J. Read and D.A. Shores: Structural characteristics of some electrodeposited aluminum-manganese alloys. *Electrochem. Technol.* **4**, 526 (1966).

37. T. Takayama, H. Seto, J. Uchida, and S. Hinotani: Local structure and concentration in Al-Mn alloy electrodeposits. *J. Appl. Electrochem.* **24**, 131 (1994).

38. W. Simon and D. Boldin: Electric equipment of an aluminum electroplating facility according to the sigal process die elektrische ausruestung einer anlage zur galvanischen abscheidung von aluminium nach dem sigal-verfahren. *Galvanotechnik* **78**, 954 (1987).

39. S. Birkle: Electrochemical deposition of aluminum. Sigal technique: Process and material properties Elektrochemische Al-Abscheidung. *MO Metalloberfläche Beschichten von Metall und Kunststoff* **42**, 511 (1988).

40. W. Fromberg and F.A.S. Donaldson: Electroplating with aluminum. *J. Appl. Manuf. Syst.* **8**, 61 (1996).

41. W. Fromberg and F.A.S. Donaldson: Electroplating with aluminum. *Adv. Mater. Processes* **149**, 33 (1996).

42. F.J. Schmidt and I.J. Hess: Properties of electroformed aluminum. *Plating* **53**, 229 (1966).

43. F.J. Schmidt and I.J. Hess: *Electroforming Aluminum for Solar Energy Concentrators*; NASA Contractor Report CR-197 (1965).

44. S.Z. El Abedin, E.M. Moustafa, R. Hempelmann, H. Natter, and F. Endres: Electrodeposition of nano- and microcrystalline aluminium in three different air and water stable ionic liquids. *ChemPhysChem* **7**, 1535 (2006).

45. E.M. Moustafa, S.Z. El Abedin, A. Shkurankov, E. Zschippang, A.Y. Saad, A. Bund, and F. Endres: Electrodeposition of Al in 1-butyl-1-methylpyrrolidinium Bis(trifluoromethylsulfonyl)amide and 1-Ethyl-3-methylimidazolium Bis(trifluoromethylsulfonyl)amide ionic liquids: In situ STM and EQCM studies. *J. Phys. Chem. B* **111**, 4693 (2007).

46. F. Endres, M. Bukowski, R. Hempelmann, and H. Natter: Electrodeposition of nanocrystalline metals and alloys from ionic liquids. *Angew. Chem. Int. Ed.* **42**, 3428 (2003).

47. H. Natter, M. Bukowski, R. Hempelmann, S.Z. El Abedin, E.M. Moustafa, and F. Endres: Electrochemical deposition of nanostructured metals and alloys from ionic liquids. *Z. Phys. Chem.* **220**, 1275 (2006).

48. S.Y. Ruan and C.A. Schuh: Electrodeposited Al-Mn alloys with microcrystalline, nanocrystalline, amorphous and nano-quasicrystalline structures. *Acta Mater.* **57**, 3810 (2009).

49. T. Fujiwara and Y. Igasaki: The effects of pulsing the current in galvanostatic electrodeposition technique on the composition and surface morphology of In-Se films. *J. Cryst. Growth* **178**, 321 (1997).

50. J. Lee, S. Farhangfar, J. Lee, L. Cagnon, R. Scholz, U. Gosele, and K. Nielsch: Tuning the crystallinity of thermoelectric Bi_2Te_3 nanowire arrays grown by pulsed electrodeposition. *Nanotechnology* **19**, (2008).

51. L. Nikolova, K. Ignatova, and S. Stefanova: Effect of pulsating electrolysis parameters on the morphology and structure of Pd-Ag powder. *J. Appl. Electrochem.* **26**, 1059 (1996).

52. M.R. Kalaniary, D.R. Gabe, and M.R. Goodenough: Unipolar and bipolar pulsed current electrodeposition for PCB production. *J. Appl. Electrochem.* **23**, 231 (1993).

53. K.P. Wong, K.C. Chan, and T.M. Yue: A study of surface finishing in pulse current electroforming of nickel by utilizing different shaped waveforms. *Surf. Coat. Technol.* **115**, 132 (1999).

54. A.C. Mishra, A.K. Thakur, and V. Srinivas: Effect of deposition parameters on microstructure of electrodeposited nickel thin films. *J. Mater. Sci.* **44**, 3520 (2009).

55. G. Saravanan and S. Mohan: Pulsed electrodeposition of microcrystalline chromium from trivalent Cr-DMF bath. *J. Appl. Electrochem.* **39**, 1393 (2009).

56. Q. Zhu and C.L. Hussey: Galvanostatic pulse plating of Cu-Al alloy in a room-temperature chloroaluminate molten salt—rotating ring-disk electrode studies. *J. Electrochem. Soc.* **148**, C395 (2001).

57. F. Giro, K. Bedner, C. Dhum, J.E. Hoffmann, S.P. Heussler, L. Jian, U. Kirsch, H.O. Moser, and M. Saumer: Pulsed electrodeposition of high aspect-ratio NiFe assemblies and its influence on spatial alloy composition. *Microsyst. Technol.* **14**, 1111 (2008).

58. J.-Y. Fei and G.D. Wilcox: Electrodeposition of Zn-Co alloys with pulse containing reverse current. *Electrochim. Acta* **50**, 2693 (2005).

59. S. Ruan and C.A. Schuh: Mesoscale structure and segregation in electrodeposited nanocrystalline alloys. *Scr. Mater.* **59**, 1218 (2008).

60. G.Y. Chin, W.F. Hosford, and W.A. Backofen: Ductile fracture of aluminum. *Trans. Metall. Soc. AIME* **230**, 437 (1964).

61. I. French and P. Weinrich: The effects of hydrostatic pressure on the mechanism of tensile fracture of aluminum. *Metall. Mater. Trans. A* **6**, 1165 (1975).

62. S. Ruan, K.L. Torres, G.B. Thompson, and C.A. Schuh: Gallium-enhanced phase contrast in atom probe tomography of nanocrystalline and amorphous Al-Mn alloys. *Ultramicroscopy* **111**, 1062 (2011).

63. H. Van Swygenhoven and P.M. Derlet: Grain-boundary sliding in nanocrystalline fcc metals. *Phys. Rev. B* **64**, 224105 (2001).

64. Z. Shan, E.A. Stach, J.M.K. Wiezorek, J.A. Knapp, D.M. Follstaedt, and S.X. Mao: Grain boundary-mediated plasticity in nanocrystalline nickel. *Science* **305**, 654 (2004).

65. Y.B. Wang, J.C. Ho, X.Z. Liao, H.Q. Li, S.P. Ringer, and Y.T. Zhu: Mechanism of grain growth during severe plastic deformation of a nanocrystalline Ni–Fe alloy. *Appl. Phys. Lett.* **94**, 011908 (2009).

66. M. Legros, D.S. Gianola, and K.J. Hemker: In situ TEM observations of fast grain-boundary motion in stressed nanocrystalline aluminum films. *Acta Mater.* **56**, 3380 (2008).

67. K.J. Hemker, D.S. Gianola, S. Van Petegem, M. Legros, S. Brandstetter, and H. Van Swygenhoven: Stress-assisted discontinuous grain growth and its effect on the deformation behavior of nanocrystalline aluminum thin films. *Acta Mater.* **54**, 2253 (2006).

68. S. Ni, Y.B. Wang, X.Z. Liao, S.N. Alhajeri, H.Q. Li, Y.H. Zhao, E.J. Lavernia, S.P. Ringer, T.G. Langdon, and Y.T. Zhu: Grain growth and dislocation density evolution in a nanocrystalline Ni-Fe alloy induced by high-pressure torsion. *Scr. Mater.* **64**, 327 (2011).

69. M. Dao, L. Lu, R.J. Asaro, J.T.M. De Hosson, and E. Ma: Toward a quantitative understanding of mechanical behavior of nanocrystalline metals. *Acta Mater.* **55**, 4041 (2007).

J. Mater. Res., Vol. 27, No. 12, Jun 28, 2012

1651